Solution Structure and Functional Characterization of SGTx1, a Modifier of Kv2.1 Channel Gating[†,‡]

Chul Won Lee,[§] Sunghwan Kim,[§] Soung Hun Roh,[§] Hiroshi Endoh,[||] Yoshio Kodera,[||] Tadakazu Maeda,[||] Toshiyuki Kohno,[⊥] Julia M. Wang,[@] Kenton J. Swartz,[@] and Jae Il Kim*[,§]

Department of Life Science, Kwangju Institute of Science and Technology, Kwangju 500-712, Korea, Department of Physics, School of Science, Kitasato University, Sagamihara, Kanagawa 228-8555, Japan, Mitsubishi Kagaku Institute of Life Sciences, 11 Minamiooya, Machida, Tokyo 194-8511, Japan, and Molecular Physiology and Biophysics Section, National Institute of Neurological Disorders and Stroke, National Institutes of Health, Bethesda, Maryland 20892

Received July 28, 2003; Revised Manuscript Received November 18, 2003

ABSTRACT: SGTx1 is a peptide toxin isolated from the venom of the spider *Scodra griseipes* that has been shown to inhibit outward K^+ currents in rat cerebellar granule neurons. Although its amino acid sequence is known to be highly (76%) homologous with that of hanatoxin (HaTx), a well-characterized modifier of Kv2.1 channel gating, the structural and functional characteristics of SGTx1 remain largely unknown. Here we describe the NMR solution structure of SGTx1, the mechanism of its interaction with Kv2.1 channels, and its effect on channel activity once bound. The NMR structure of SGTx1 contains a molecular fold closely resembling the "inhibitor cystine knot" of HaTx, which is composed of an antiparallel β-sheet and four chain reversals stabilized by three disulfide bonds. Functionally, SGTx1 reversibly inhibited K^+ currents in oocytes expressing Kv2.1 channels. Moreover, generation of steady-state activation curves showed that, consistent with other gating modifiers, SGTx1 acted by shifting the activation of the channel to more depolarized voltages. Thus, the surface profile and mechanism of action of SGTx1 are similar to those of HaTx. Still, detailed comparison of SGTx1 with HaTx revealed differences in binding affinity and conformational homogeneity that result from differences in the charge distribution at the binding surface and in the amino acid composition of the respective β-hairpin structures in the peptides.

Voltage-gated ion channels are expressed by many cells and play a crucial role in regulating membrane potential and various cellular functions. A variety of peptide toxins isolated from the venom of spiders, scorpions, and cone snails, among others, functionally inhibit voltage-gated ion channels and have proven to be valuable pharmacological tools for evaluating specific channel characteristics. Moreover, determination of structures of these toxins has provided a foundation for investigating the molecular basis of toxin affinity and specificity and for drug development directed against ion channel-related diseases.

Although the origins of venomous peptide toxins that interact with voltage-gated ion channels are diverse, their modes of action fall into two major categories: pore blockers and gating modifiers. Pore-blocking toxins bind to the external vestibule of the channel and physically obstruct the movement of ions by occluding the ion-conducting pore (*1*). The three-dimensional structures of many pore-blocking toxins, including the μ-conotoxins for the Na^+ channel, charybdotoxin for the K^+ channel, and ω-conotoxins for the Ca^{2+} channel, have all been determined, enabling analysis of the structure−activity relationships between pore blockers and voltage-gated ion channels (*2*−*7*). Gating modifiers, on the other hand, bind close to the channel voltage sensor and alter the energetics of voltage-dependent gating (*8*−*12*). The structures of several Na^+ channel gating modifiers, including the α- and β-scorpion toxins and sea anemone toxins, have been determined (*13*, *14*), as have the solution structures of ω-agatoxin IVA and ω-grammotoxin SIA (GrTx) for the Ca^{2+} channel and hanatoxin (HaTx) for the K^+ channel (*15*−*17*). Comparison of the structures of the Na^+, Ca^{2+}, and K^+ channel gating modifiers suggests that a conserved motif consisting of a hydrophobic patch surrounded by positively charged residues might be functionally important for the binding of these peptides (*16*).

SGTx1 is a 34-amino acid peptide recently isolated from the venom of the spider *Scodra griseipes* that is reported to reversibly inhibit outward K^+ channel currents in rat cerebellum granular cells (*18*). Although relatively little is known about the interaction of SGTx1 with specific types of K^+ channels, it shows the highest degree of sequence identity

[†] This study was supported by grants from the Ministry of Science and Technology, Korea, from the Korea Science and Engineering Foundation through the Research Center for Proteinaceous Materials, and from the Brain Korea 21 program, and in part by Grants-in-Aid for Scientific Research on Priority Areas "Medical Genome Science" from the Ministry of Education, Culture, Sports, Science, and Technology of Japan (Y.K. and T.M.) and Kitasato University Research Grants for Young Researchers (H.E. and Y.K.).

[‡] Atomic coordinates for the 20 converged structures of SGTx1 have been deposited in the Protein Data Bank as entry 1LA4.

* To whom correspondence should be addressed: Department of Life Science, Kwangju Institute of Science and Technology, Kwangju 500-712, Korea. E-mail: jikim@kjist.ac.kr. Phone: +82-62-970-2494. Fax: +82-62-970-2553.

[§] Kwangju Institute of Science and Technology.

[||] Kitasato University.

[⊥] Mitsubishi Kagaku Institute of Life Sciences.

[@] National Institutes of Health.

10.1021/bi0353373 CCC: $27.50
Published on Web 01/03/2004

with several more fully characterized spider toxins, including HaTx (76%), SNX-482 (60%), TxP5 toxin (32%), and huwentoxin (26%). HaTx, which is a 35-amino acid toxin from the venom of the Chilean tarantula *Grammoatola spatulata*, modulates the function of the Kv2.1 voltage-gated K^+ channel (*19*) and is the first known gating modifier that interacts with the voltage-sensing domain of a voltage-gated K^+ channel (*8*−*10*). Unfortunately, HaTx is rare in nature, and its chemical synthesis is difficult, primarily because the yield in the folding step is very low (∼1%). Consequently, the utility of this toxin as a pharmacological or electrophysiological probe for studying the gating mechanism of K^+ channels has been limited.

In the study presented here, we have chemically synthesized SGTx1 in amounts sufficient for NMR[1] studies and determined its solution structure using proton NMR spectroscopy with dynamical simulated annealing calculations. The NMR structure of SGTx1 closely resembles that of HaTx and shows the unique structural characteristic of gating modifiers, including the hydrophobic patch surrounded by positively charged residues. On the basis of structural and electrophysiological analyses, we strongly suggest that SGTx1 acts in a manner similar to that of HaTx to modify Kv2.1 channel gating.

MATERIALS AND METHODS

Peptide Synthesis and Disulfide Bond Determination. Peptide synthesis was conducted on an Applied Biosystems model 433A peptide synthesizer. The linear precursor of SGTx1 was synthesized using a solid-phase methodology with Fmoc chemistry, starting from Fmoc-Phe-Alko resin using a variety of blocking groups for the protection of the amino acids. After trifluoroacetic acid cleavage, a crude linear peptide was extracted with 2 M acetic acid and diluted to a final concentration of 25 μM. A solution containing 0.1 M ammonium acetate, 2 M urea, 2.5 mM reduced glutathione, and 0.25 mM oxidized glutathione was adjusted to pH 7.8 with aqueous NH_4OH and stirred slowly at 4 °C for 3 days. The folding reaction was monitored with RP-HPLC, and the crude oxidized product was purified by successive chromatography steps with CM-cellulose CM-52 and preparative RP-HPLC with a C18 silica column. The purity of the synthetic SGTx1 was confirmed by analytical RP-HPLC and MALDI-TOF MS measurements.

The disulfide bond pairings of synthetic SGTx1 were determined using a method similar to that used to determine the disulfide bond pairings of ω-conotoxin TxVII (*20*). The authentic peptide TCR/TTADCCK/SDGKYCAWDGTF, which is connected by two definite disulfide bonds, was synthesized for comparison with the fragment excised from SGTx1 by trypsin digestion.

NMR Spectroscopy. NMR measurements were carried out using standard pulse sequences and phase cycling on a Bruker DMX-500 or DRX 600 spectrometer. Samples for NMR experiments were 2 mM SGTx1 dissolved in either a 90% H_2O/10% ^2H_2O mixture or 99.96% ^2H_2O at pH 3.5 (uncorrected for the isotope effect). All two-dimensional NMR spectra were acquired in a phase-sensitive mode using time-proportional phase incrementation (*21*) for quadrature detection in the t_1 dimension at temperatures of 301 and 310 K. TOCSY spectra were recorded using a MLEV-17 pulse scheme (*22*) with isotropic mixing times of 60 and 80 ms. NOESY spectra (*23*, *24*) were recorded with mixing times of 80, 150, and 250 ms. Suppression of the solvent resonance in both the NOESY and TOCSY measurements was achieved using the WATERGATE scheme (*25*). DQF-COSY (*26*) and PE-COSY (*27*) spectra were recorded to obtain the constraints for the torsion angles and stereospecific assignments, respectively. In this case, solvent resonance was suppressed by selective irradiation during the relaxation delay period. The data sizes used for acquisition were 512 (t_1) × 8192 (t_2) for DQF-COSY and PE-COSY and 512 × 2048 otherwise. Slowly exchanging backbone amide protons were identified by analysis of TOCSY spectra recorded in 99.96% ^2H_2O on time scales of 30 min and 3.5 h and then every 3 h up to 25 h.

Chemical shifts were referenced to the methyl resonance of DSS used as an internal standard. Complete sets of two-dimensional spectra were recorded at 310 K and pH 3.5.

Spectra were processed with UXNMR or XWIN NMR software. Phase-shifted sine-squared window functions were applied before Fourier transformation. Except for that for PE-COSY, final matrix sizes were 2048 × 2048 real points. High-resolution DQF-COSY and PE-COSY spectra were strip transformed to 1024 × 8192 points.

Experimental Restraints and Structure Calculations. Quantitative determination of the cross-peak intensities was based on the counting levels. Observed NOE data were classified into four distance ranges: 1.8−2.7, 1.8−3.5, 1.8−5.0, and 1.8−6.0 Å, corresponding to strong, medium, weak, and very weak NOE values, respectively. Pseudoatoms were used for the methyl protons or the non-stereospecifically assigned methylene protons (*28*). Correcting factors for the use of pseudoatoms were added to the distance constraints, and 0.5 Å was added to the distance constraints involving methyl protons (*29*). For each disulfide bond, we used three distance constraints, S(i)−S(j), S(i)−C$^\beta$(j), and S(j)−C$^\beta$(i), whose target values were set to 2.02 ± 0.02, 2.99 ± 0.5, and 2.99 ± 0.5 Å, respectively (*30*).

The backbone NH−C$^\alpha$H coupling constants were estimated from the DQF-COSY spectrum and were converted to backbone torsion angle ϕ constraints according to the following rules. For $^3J_{NH-C^\alpha H}$ values of <5.5 Hz, the ϕ angle was constrained in the range of −65 ± 25°; for $^3J_{NH-C^\alpha H}$ values of >8.0 Hz, it was constrained in the range of −120 ± 40° (*31*, *32*). Backbone dihedral constraints were not applied to $^3J_{NH-C^\alpha H}$ values between 5.5 and 8.0 Hz. The range of the χ^1 side chain torsion angle constraints and the stereospecific assignment of the prochiral β-methylene protons were obtained by using the $^3J_{\alpha\beta}$ coupling constants combined with the intraresidue NH−C$^\beta$H NOEs (*33*). The $^3J_{\alpha\beta}$ coupling constants were determined from the PE-COSY spectrum in ^2H_2O. For the t^2g^3, g^2g^3, and g^2t^3 conformations around the C$^\alpha$−C$^\beta$ bonds, the χ^1 side chain torsion angle was constrained in the ranges of −60 ± 30°, 60 ± 30°, and

[1] Abbreviations: DQF-COSY, double-quantum-filtered correlation spectroscopy; DSS, 4,4-dimethyl-4-silapentane-1-sulfonic acid; Fmoc, 9-fluorenylmethoxycarbonyl; MALDI-TOF MS, matrix-assisted laser desorption/ionization time-of-flight mass spectrometry; NOE, nuclear Overhauser effect; NOESY, NOE spectroscopy; NMR, nuclear magnetic resonance; PE-COSY, primitive exclusive correlation spectroscopy; PDB, Protein Data Bank; rms, root-mean-square; RP-HPLC, reversed-phase high-performance liquid chromatography; TFA, trifluoroacetic acid; TOCSY, total correlation spectroscopy.

180 ± 30°, respectively (*34*). The hydrogen bond acceptors for the slowly exchanged amide protons were identified by analyzing the preliminary calculated structures (*35*, *36*). The distance restraints of hydrogen bonds were added as target values of 1.8−2.3 Å for NH(*i*)−O(*j*) bonds and 2.8−3.3 Å for N(*i*)−O(*j*) bonds.

All calculations were carried out on an SGI O2 workstation using the X-PLOR 3.851 program (*37*). The three-dimensional structures were calculated on the basis of the experimentally derived distance and torsion angle constraints using a dynamically simulated annealing protocol starting from a template structure with randomized backbone ϕ and ψ torsion angles.

Evaluation of the Structure. The final 20 structures with the lowest energy and smallest Lennard-Jones van der Waals energy were chosen. The convergence of the calculated structures was evaluated in terms of the structural parameters. There were rms deviations from the experimental distance and dihedral constraints, from the energetic statistics (F_{NOE}, F_{tor}, F_{repel}, and E_{L-J}), and from the idealized geometry. The structures were analyzed using PROCHECK_NMR (*38*), PROMOTIF (*39*), and MOLMOL (*40*). The distributions of the backbone dihedral angles in the final converged structure were evaluated by representation of the Ramachandran dihedral pattern, which indicated the deviations from the allowed ϕ and ψ angle limits. The degrees of angular variation among the converged structures were further assessed by using an angular order parameter (*5*, *41*). The solvent accessible surface areas for the side chains of amino acid residues were calculated with a solvent radius of 1.4 Å.

Functional Characterization of Synthetic SGTx1. The capacity of synthetic SGTx1 to inhibit the activity of the Kv2.1Δ7 channel (*42*) was examined in *Xenopus* oocytes. Kv2.1Δ7 contains seven mutations in the S5−S6 linker (*43*, *44*), which render the channel sensitive to the pore-blocking toxin Agitoxin-2, enabling it to be used to subtract background conductances. Kv2.1 cDNA in the pBlu-SK− vector was linearized with *Not*I and transcribed using T7 RNA polymerase. *Xenopus laevis* oocytes were removed surgically and incubated with agitation for 1−1.5 h in a solution containing 82.5 mM NaCl, 2.5 mM KCl, 1 mM $MgCl_2$, 5 mM HEPES, and 2 mg/mL collagenase (Worthington Biochemical Corp.); the pH was adjusted to 7.6 with NaOH. Defolliculated oocytes were injected with cRNA and incubated at 17 °C in a solution containing 96 mM NaCl, 2 mM KCl, 1 mM $MgCl_2$, 1.8 mM $CaCl_2$, 5 mM HEPES, and 50 μg/mL gentamicin (Invitrogen/GIBCO BRL); the pH was adjusted to 7.6 with NaOH.

Between 1 and 3 days after the injection of cRNA, macroscopic ionic currents from oocytes expressing the Kv2.1Δ7 channel were recorded using the two-electrode voltage clamp techniques with an OC-725C oocyte clamp (Warner Instruments). Oocytes were studied in a 200 μL recording chamber that was perfused with a solution containing 50 mM RbCl, 50 mM NaCl, 1 mM $MgCl_2$, 0.3 mM $CaCl_2$, and 5 mM HEPES; the pH was adjusted to 7.6 with NaOH. Microelectrode resistances were 0.2−1.2 MΩ when oocytes were filled with 3 M KCl. All experiments were carried out at room temperature (~22 °C). Recorded data were filtered at 2 kHz (8-pole Bessel) and digitized at 10 kHz. Linear capacity, leak, and endogenous currents were subtracted after the Kv2.1 channel had been blocked with 1.25 μM Agitoxin-2 (Alomone Labs) (*45*). The concentration of synthetic SGTx1 was determined using an extinction coefficient of 8.6×10^3 M^{-1} cm^{-1} at 280 nm.

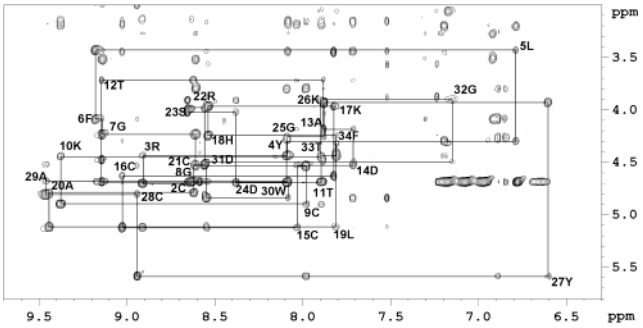

FIGURE 1: Sequential $d_{\alpha N}(i, i+1)$ NOE connectivities for residues 2−34 in the NOESY spectrum observed with a mixing time of 250 ms at 310 K. Intraresidue NH−C$^{\alpha}$H cross-peaks are labeled with the residue number using standard single-letter amino acid abbreviations.

RESULTS AND DISCUSSION

Synthesis of SGTx1. Because it is a cyclic peptide with multiple disulfide bonds, the synthesis of SGTx1 was not as straightforward as it would have been for a linear peptide. Nevertheless, controlled air oxidation of a linear precursor yielded satisfactory amounts of a single major compound on RP-HPLC that was cyclized by native-type disulfide pairings and was thus fully active. The disulfide bond pairings of the synthetic SGTx1, which were determined by combined analysis of the fragments produced by enzymatic digestion and regioselective peptide synthesis, proved to be the same as those of native SGTx1 (*18*), namely, Cys2−Cys16, Cys9−Cys21, and Cys15−Cys28.

NMR Analysis. Complete proton resonance assignments for SGTx1 were determined using traditional two-dimensional NMR sequential assignment techniques (*46*). Identification of the amino acid spin system was based on scalar coupling patterns observed in DQF-COSY and TOCSY experiments, complemented by the results of NOESY measurements. The identified spin systems were ordered along the primary structure of SGTx1 through interresidue sequential NOEs observed on the NOESY spectrum. Figure 1 shows the NH−C$^{\alpha}$H fingerprint region of the NOESY spectrum, which contains sequential $d_{\alpha N}(i, i+1)$ connectivity. The pattern of observed NOEs was ultimately interpreted in terms of the secondary structure of the molecule. As summarized in Figure 2, SGTx1 contains three short β-strands comprised of residues 7−9, 19−22, and 27−30, which are arranged in antiparallel fashion with several turns. The extent of the β-strands and their relative orientation in the β-sheet structure were determined using standard criteria: large $^3J_{HN\alpha}$ coupling constants (Ala20, Tyr27, and Ala29), strong sequential $d_{\alpha N}$, interstrand NH−NH and NH−C$^{\alpha}$H connectivities, and slowly exchanging amide protons (Cys9, Ala20, Arg22, Tyr27, Cys28, and Ala29). These criteria enabled discrimination of the peripheral and central strands within the β-sheet.

Calculation of the Solution Structure of SGTx1. We used a total of 499 NMR experimental constraints to calculate the three-dimensional structure of SGTx1, including 472 experimental distance constraints and 27 dihedral angle

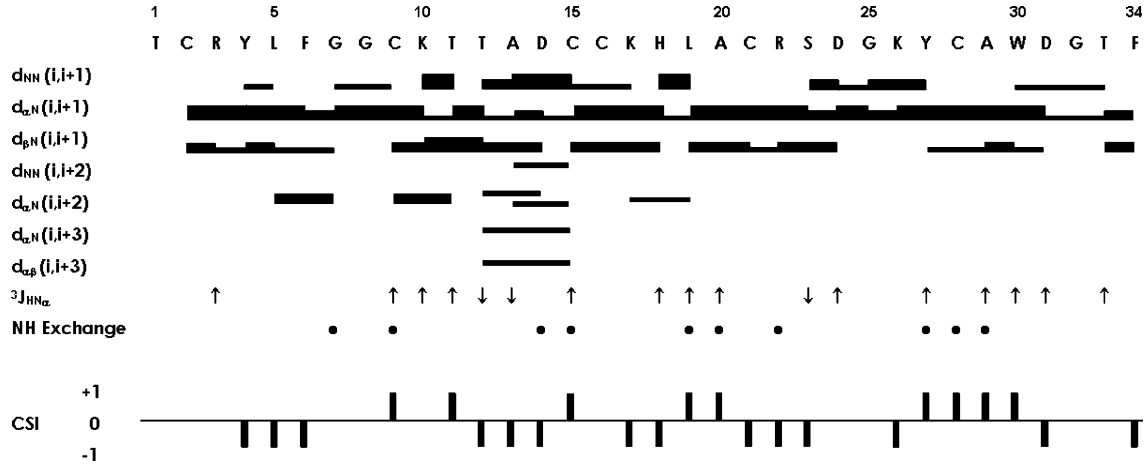

FIGURE 2: Summary of the sequential and medium-range NOE connectivities, $^3J_{NH-C^\alpha H}$ coupling constants, and slowly exchanging backbone NH protons observed in SGTx1. These structural parameters were used for sequence specific assignments and for identification of secondary structural elements. Sequential and medium-range NOEs, d_{NN}, d^{α}_{N}, d^{β}_{N}, $d_{NN}(i, i + 2)$, $d^{\alpha}_{N}(i, i + 2)$, $d^{\alpha}_{N}(i, i + 3)$, and $d_{\alpha\beta}(i, i + 3)$, are indicated by bars between two residues. The classification of NOEs as strong, medium, or weak is indicated by the height of the filled bars. Values of the $^3J_{NH-C^\alpha H}$ coupling constants are indicated with ↑ ($\geq$8 Hz) and ↓ ($\leq$5.5 Hz). Filled circles denote backbone amide protons that were still observed in the TOCSY spectra after 25 h in ^2H_2O. The chemical shift index is indicated by a ternary index with a value of −1, 0, or 1. Values of −1 and 1 indicate a shift deviation from the random-coil value of greater than 0.1 ppm upfield and downfield, respectively; those within the range of random-coil values are given a value of 0 (*56*).

constraints, which corresponds to an average of 14.7 constraints per residue. Of the 472 distance constraints, there were 173 intraresidue constraints, 276 interresidue NOE distance constraints, 14 hydrogen bond constraints determined from hydrogen−deuterium exchange-out experiments, and nine disulfide bond constraints. The 14 distance constraints related to hydrogen bonds are as follows: Cys9(HN)−Lys26(CO), Cys15(HN)−Thr12(CO), Ala20(HN)−Ala29(CO), Arg22(HN)−Tyr27(CO), Tyr27(HN)−Arg22(CO), Cys28(HN)−Gly7(CO), and Ala29(HN)−Ala20(CO).

We carried out the simulated annealing calculations starting with 100 random SGTx1 structures, and selected 20 final structures that were in good agreement with the NMR experimental constraints, for which the NOE distance and torsion angle violations were smaller than 0.3 Å and 3°, respectively. Statistics for the converged structures were evaluated in terms of structural parameters (Table 1). The deviations from the idealized covalent geometry were very small, and the Lennard-Jones van der Waals energy was large and negative, indicating that there are no distortions or nonbonded bad contacts in the converged structures. The atomic rms deviation about the mean coordinate positions for residues 2−30 was 0.23 ± 0.04 Å for the backbone atoms (N, C^α, and C) and 1.18 ± 0.15 Å for all heavy atoms. As shown in Figure 3, the backbone structures for residues 2−30 were well-defined in the converged structures; Ramachandran analysis showed that the backbone dihedral angles fall either within the β-sheet region or in generally allowed regions. The N-terminal residue (Thr1) and the C-terminal segment (Asp31−Phe34) were not restricted by NMR constraints, reflecting the randomness of the conformationally disordered backbone. This may be the result of a lack of medium- and long-range NOE constraints due to the inherent flexibility of both segments.

Molecular Structure of SGTx1. The molecular structure of SGTx1 consists of a triple-stranded antiparallel β-sheet and four chain reversals. The overall β-sheet topology of SGTx1 is +2*x*, −1, which is frequently associated with toxic and inhibitory peptides having an "inhibitor cystine knot" fold (*47*−*49*). The three β-strands are formed by residues Gly7−Cys9 (β-strand I), Leu19−Arg22 (β-strand II), and Tyr27-Trp30 (β-strand III), with β-strand I tethered to β-strand II by a disulfide bond (Cys9−Cys21) and interacting with the central β-strand III in antiparallel fashion at an angle of ~45° (Figure 4A). The first chain reversal occurs at residues Tyr4−Gly7, which form a type II β-turn. The presence of a phenylalanine residue (Phe6) with a positive ϕ value at position $i + 2$ of a type II β-turn is not common, but this one showed a $^3J_{HN^\alpha}$ coupling constant of ap-

Table 1: Structural Statistics for the Final 20 Structures of SGTx1

rms deviation from experimental distance constraints (Å)[a] (472)	0.0194 ± 0.0005
rms deviation from experimental dihedral constraints (deg)[a] (27)	0.43619 ± 0.1177
energetic statistics (kcal/mol)[b]	
F_{NOE}	8.8807 ± 0.5004
F_{tor}	0.3503 ± 0.1806
F_{repel}	3.8885 ± 0.7399
E_{L-J}	−88.0863 ± 8.3166
rms deviation from idealized geometry	
bonds (Å)	0.0020 ± 0.0001
angles (deg)	0.5347 ± 0.0088
impropers (deg)	0.4070 ± 0.0005
Ramachandran analysis (%) (residues 2−30)[c]	
most favored regions	57.10
additionally allowed regions	37.30
generously allowed regions	5.60
disallowed regions	0.00
average rms deviations (Å) (residues 2−30)	
backbone (N, C^α, and C)	0.23 ± 0.04
all heavy atoms	1.18 ± 0.15

[a] The number of each experimental constraint used in the calculations is given in parentheses. [b] F_{NOE}, F_{tor}, and F_{repel} are the energies related to the NOE violations, the torsion angle violations, and the van der Waals repulsion term, respectively. The values of the force constants used for these terms are the standard values as depicted in the X-PLOR 3.1 manual (*37*). E_{L-J} is the Lennard-Jones van der Waals energy calculated with the CHARMm empirical energy function (*57*). E_{L-J} was not used in the dynamical simulated annealing calculations. [c] The program PROCHECK_NMR (*38*) was used to assess the stereochemical quality of the structures.

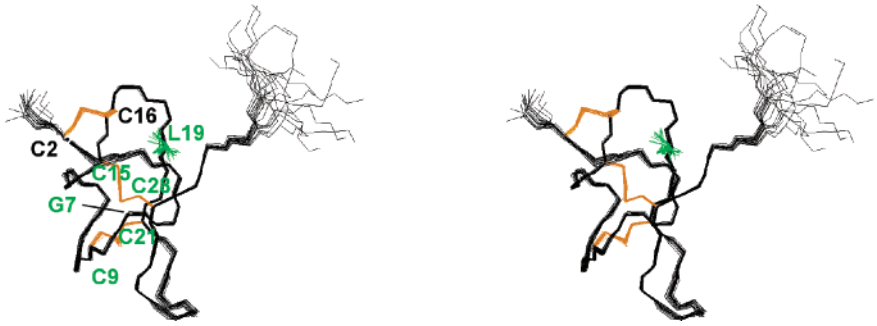

FIGURE 3: Stereopairs of backbone heavy atoms (N, C^{α}, and C) for the 20 converged structures of SGTx1. These are the results of the best-fit superposition of the backbone heavy atoms in the central part (residues 2−30) of the molecule. Disulfide bonds are shown and colored orange. The backbone regions of the central core residues (Gly7, Cys9, Cys15, Leu19, Cys21, and Cys28) are labeled with green characters. The side chain of Leu19 is shown in green. This figure was generated using MOLMOL.

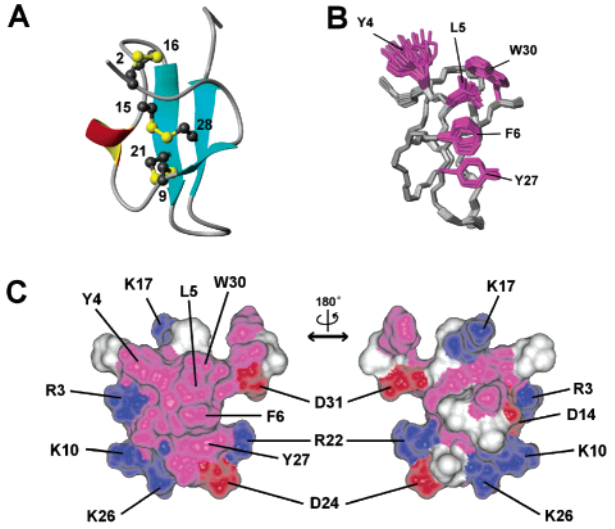

FIGURE 4: Solution structure of SGTx1. (A) Schematic diagram of SGTx1 illustrating the location of the β-strands (cyan), the 3_{10}-helical turn (red and yellow), and the disulfide bonds (numbered ball-and-stick diagram). (B) Backbone heavy atoms (N, C^{α}, and C) for the 20 converged structures of the central part (residues 2−30) of the molecule. The side chains of the surface hydrophobic patch residues (Tyr4, Leu5, Phe6, Tyr27, and Trp30) are shown in purple. (C) Surface profile of SGTx1. The left and right figures are rotated 180° relative to one another about a vertical axis. Hydrophobic residues (Ala, Cys, Leu, Phe, Trp, and Tyr) are colored purple; basic (Arg and Lys) and acidic (Asp) residues are colored blue and red, respectively. The other residues are colored white. The surface hydrophobic patch residues (Tyr4, Leu5, Phe6, Tyr27, and Trp30) and charged residues (Arg3, Lys10, Asp14, Lys17, Arg22, Asp24, Lys26, and Asp31) are indicated.

proximately 7 Hz and a very strong intraresidual NH−C^{α}H NOE, which is consistent with the structural characteristics of the positive ϕ angle that was observed by NMR spectroscopy. Notably, a positive ϕ angle at position $i + 2$ of a type II β-turn was also observed in HaTx and ω-agatoxin IVA and IVB. The second and third reversals occur at residues Thr12−Asp14 and Cys16−Leu19, which form a 3_{10}-helical turn and a type IV β-turn (miscellaneous type), respectively. As shown in Figure 2, the segment from Thr12 to Cys15 exhibits the characteristic NOE connectivities of a 3_{10}-helix structure, together with slowly exchanging amide protons (Asp14 and Cys15). The final reversal occurs at residues Ser23−Lys26 and forms a β-hairpin turn (a type IV β-turn) that reverses the direction of the backbone between β-strands II and III.

Surface Profile. In the converged structure of SGTx1, two disulfide bonds, Cys9−Cys21 and Cys15−Cys28, together with the side chain of Leu19, show very low solvent accessibility (<5%) and form the hydrophobic core of the molecule. On the surface of SGTx1 are five positively charged basic residues (Arg3, Lys10, Lys17, Arg22, and Lys26), three negatively charged acidic residues (Asp14, Asp24, and Asp31), and, interestingly, several hydrophobic residues that are highly exposed to the solvent (Tyr4, Leu5, Phe6, Tyr27, and Trp30) (Figure 4C). With the exception of Tyr4, the four solvent-exposed hydrophobic residues are stacked in line with one another on one face of the structure and form a significant profile on the surface of SGTx1 (Figure 4B). The orientations of the surface aromatic rings of Phe6, Tyr27, and Trp30 are well-defined with Leu5 sandwiched between the phenyl ring of Phe6 and the indole ring of Trp30; the phenyl ring of Phe6 induces a "tilted" stacking of the phenolic ring of Tyr27 (*50*). In the NMR spectra, the backbone amide proton and γ-proton resonances originating from Leu5 were observed at unusual positions (6.78 and 0.35 ppm, respectively) due to a ring current shift in Trp30. The five basic and three acidic residues are arranged around the edge of the surface hydrophobic patch (Figure 4C), and we previously pointed out that the surface motif comprised of a hydrophobic patch surrounded by positively charged residues is likely the region used by gating modifier toxins in binding to voltage-gated ion channels (*16*). That SGTx1 also adopts this surface profile raises the possibility that it binds to the voltage-sensing domain in voltage-gated K^+ channels in a manner similar to that of HaTx.

Functional Characterization of Synthetic SGTx1. Native SGTx1 has been shown to inhibit voltage-gated K^+ currents in cerebellar granule neurons (*18*). Although relatively little is known about the interaction of SGTx1 with specific K^+ channel types, because the primary and tertiary structures of SGTx1 are very similar to HaTx, we focused on the interaction between synthetic SGTx1 and the Kv2.1 channel, which was expressed in *Xenopus* oocytes and studied using the two-electrode voltage clamp technique. To initially evaluate the effects of SGTx1, the Kv2.1 channel was activated by weak depolarizations of the membrane while the toxin was being added to the recording chamber. The synthetic toxin inhibited K^+ currents by ~75% when applied at a concentration of 500 nM (Figure 5A,B). This effect was reversible, and the voltage-activated currents recovered to control levels after removal of the toxin from the recording chamber (Figure 5B).

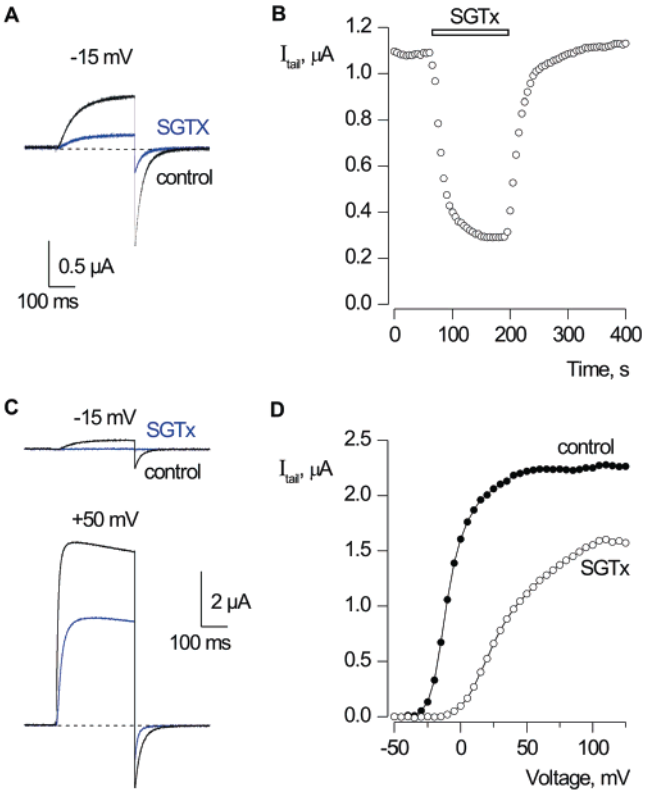

FIGURE 5: Inhibition of the Kv2.1Δ7 channel by synthetic SGTx1. (A) Voltage-clamp recording from an oocyte expressing the Kv2.1Δ7 channel. Currents were elicited by depolarization to −15 mV in the absence (black trace) or presence (blue trace) of 500 nM SGTx1. The holding voltage was −90 mV, and the tail voltage was −50 mV. The dashed line indicates the level of zero current. Leak, background, and capacitive currents were subtracted after the channel had been blocked with Agitoxin-2. (B) Time course of inhibition of the Kv2.1Δ7 channel by 500 nM SGTx1 in the same cell as that described for panel A. Depolarizations were elicited every 5 s. (C) Current records elicited by weak (−15 mV) and strong (50 mV) depolarizations in the absence (black trace) and presence (blue trace) of 2 μM SGTx1. The holding voltage was −90 mV, and the tail voltage was −50 mV. The subtraction protocol was the same as that described for panel A. Single-exponential fits to tail currents following depolarization to 50 mV yielded a τ of 25.4 ms under control conditions and 11 ms in the presence of SGTx1. (D) Voltage activation relations in the absence and presence of 2 μM SGTx1. Tail currents obtained following depolarizations of various strength were averaged for 0.3 ms beginning 2.3 ms after repolarization to −50 mV.

One indication that HaTx inhibits the Kv2.1 channel by modifying its gating is that the toxin shifts the steady-state activation of the channel to more depolarized voltages (*20*); i.e., toxin-bound channels can open, but only when the membrane is sufficiently depolarized. To test whether SGTx1 inhibits the Kv2.1 channel by a similar mechanism, we generated activation curves for the Kv2.1 channel in the absence and presence of 2 μM SGTx1 (Figure 5D). Like HaTx, SGTx1 shifted activation of the channel to more depolarized voltages. Although the toxin completely inhibits currents activated by weak depolarization to −15 mV, the channel can be opened by stronger depolarizations to 50 mV (Figure 5C). Moreover, our finding that channels opened by strong depolarization are deactivated much faster in the presence of SGTx1 (τ = 11 ms) than in a control solution (τ = 25 ms) suggests that the toxin remains bound to the channel as it opens and closes. All of these effects of SGTx1 are similar to what has been seen previously with HaTx and the Kv2.1 channel, suggesting that the two toxins share a common mechanism.

Structure−Activity Relationships of SGTx1 and HaTx. The structural and functional studies summarized so far indicate that, like HaTx, SGTx1 is a modifier of Kv2.1 channel gating. That SGTx1 interacts with the Kv2.1 channel with a lower affinity ($K_d \sim 2$ μM) than HaTx (K_d = 160 nM) is indicative of a subtle difference in the active sites of the two toxins. In Figure 6, we compared the orientations of the residues within the hydrophobic patch and the surrounding charged residues on the surfaces of SGTx1 and HaTx and the Ca^{2+} channel gating modifier GrTx. Despite differences in channel affinity and specificity, the three toxins show substantial similarity in their three-dimensional structures; i.e., all three exhibit the inhibitor cystine knot motif. From the detailed comparison of the structures, we understand that SGTx1 interacts with the Kv2.1 channel in a manner similar to that of HaTx. The proposed active site of HaTx, which consists of five hydrophobic surface residues (Tyr4, Leu5, Phe6, Tyr27, and Trp30) surrounded by three basic residues (Lys22, Arg24, and Lys26) and two acidic residues (Asp25 and Asp31), is nearly conserved in SGTx1. The surface hydrophobic residues of SGTx1 are well-defined with a χ^1 angular order parameter of >0.962. In particular, the indole ring of Trp30 shows rms deviations for all heavy atoms of only 0.07 ± 0.04 Å and a χ^1 angular order parameter of 1.0. In an earlier report, we suggested that the difference in the orientation of the indole rings of Trp30 of HaTx and Trp32 of GrTx might account for the difference in the binding affinities of HaTx and GrTx for voltage-gated K^+ and Ca^{2+} channels. In GrTx, the aromatic−aromatic interaction and the atomic contact between Phe5 and Trp32 make the conformation of Trp32 an "open" one. In HaTx, by contrast, Phe5 of GrTx is replaced by Leu5, which interacts with Trp30, giving it a "closed" conformation (*17*); likewise, Trp30 in SGTx1 assumes a closed conformation (Figure 6), which likely contributes to the biological similarity between SGTx1 and HaTx with respect to Kv2.1 channels.

Mutational scanning studies of the interaction between the Kv2.1 channel and HaTx revealed that two hydrophobic residues (Ile273 and Phe274) and an acidic residue (Glu277) in the C-terminus of the S3 segment of the channel are important for its binding with HaTx (*9*). Both scanning mutagenesis studies of the Kv2.1 channel (*51*) and the X-ray structure of the KvAP channel (*52*) suggest that the C-terminus of the S3 segment adopts an α-helical secondary structure in which three residues (Ile273, Phe274, and Glu277) closely lie on the one side of helical surface. Therefore, one possibility is that Ile273 and Phe274 interact with the surface hydrophobic residues of HaTx, while Glu277 interacts with one or more of the three basic residues (Lys22, Arg24, and Lys26) that surround the hydrophobic patch. Two basic residues (Arg22 and Lys26) surround the hydrophobic patch of SGTx1, one fewer than in HaTx (Figure 6). Comparison of the primary sequences of SGTx1 and HaTx indicates that they differ at nine positions, though only three of those are located at the proposed binding site. Lys22 and Asp25 in HaTx are replaced in SGTx1 by Arg22 and Asp24, respectively, which have similar characteristics. This means that the distinctive difference in the active sites of SGTx1 and HaTx is the absence of Arg24 in SGTx1. In previous molecular simulations and docking studies, Arg24 of HaTx formed an intermolecular salt bridge with Glu277 of the

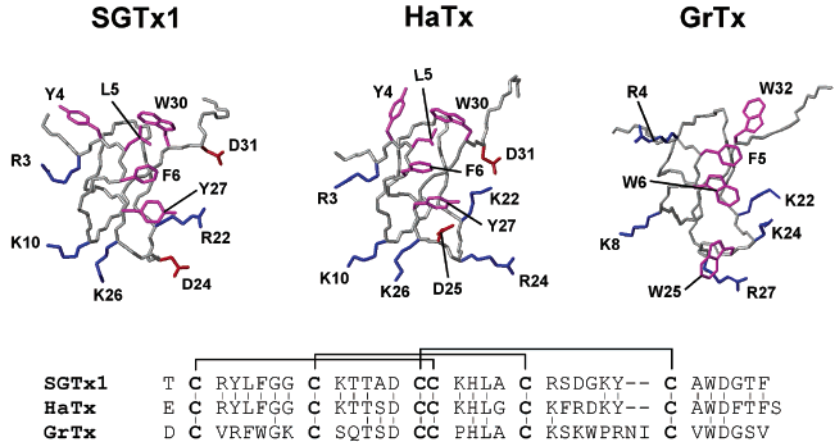

FIGURE 6: Comparison of the surface hydrophobic patches and some interesting charged residues in SGTx1, HaTx, and GrTx. Hydrophobic residues are colored purple; basic and acidic residues are colored blue and red, respectively. The coordinates of HaTx and GrTx were obtained from PDB entries 1D1H and 1KOZ, respectively. Amino acid sequences of SGTx1, HaTx, and GrTx are illustrated at the bottom. Cysteine residues are shown in bold letters, and disulfide connectivities are represented as lines.

Kv2.1 channel, and an intramolecular salt bridge with Asp25 (*53*, *54*). Thus, the presence or absence of Arg24 in HaTx or SGTx1, respectively, may explain the difference in the binding affinities of these two toxins for Kv2.1 channels.

Origin of the Conformational Heterogeneity of HaTx. Two observations suggest that HaTx exhibits conformational heterogeneity. First, HaTx elutes as two peaks when purified using analytical HPLC (Figure 7A). Collection and reinjection of either peak gives rise to the same double (*19*), suggesting that the two forms of the toxin equilibrate in solution. Second, resonances originating from 15 residues in the NMR spectra of HaTx were observed as double peaks (*16*). In contrast, for SGTx1 only one peak is observed in the HPLC purification (Figure 7A) and no double-peak resonances are observed in the NMR spectrum (Figure 1). One possibility is that the conformational heterogeneity in HaTx is due to rotational isomerization of a disulfide bond, as previously suggested (*16*). However, comparison of the primary and tertiary structures of HaTx and SGTx1 reveals that although the overall topologies are similar, there are several differences in their backbone structures that might give rise to the apparently unique conformational heterogeneity that is observed for HaTx. The backbone of SGTx1 is composed of three β-strands (residues 7−9, 19−22, and 27−30) and four chain reversals, whereas HaTx is missing the first β-strand; β-strands II and III (residues 19−21 and 28−30, respectively), which comprise a β-hairpin structure, are shorter than those of SGTx1 (Figure 7B). In addition, among the four chain reversals in HaTx, the fourth is poorly defined (*16*), while that of SGTx1 is well-defined and has a type IV β-turn structure (Figure 7B). The overall stability of a hairpin structure depends on many factors, including backbone hydrogen bonding, the secondary structural propensities of the different amino acids, and interstrand side chain−side chain interactions. Analysis of a series of peptides based on the de novo design of the β-hairpin peptide (BH8) showed that they all contain the Xxx-Gly sequence in the turn region, with Xxx being Asn, Asp, Ser, Ala, or Gly (*55*). Interestingly, SGTx1 adopts the common Xxx-Gly (Asp24-Gly25) sequence in the hairpin turn, but HaTx does not. In addition, Gly20 of HaTx is substituted with a more hydrophobic residue (Ala20) in the first β-strand of the hairpin structure in SGTx1. This may lead to an interstrand side chain

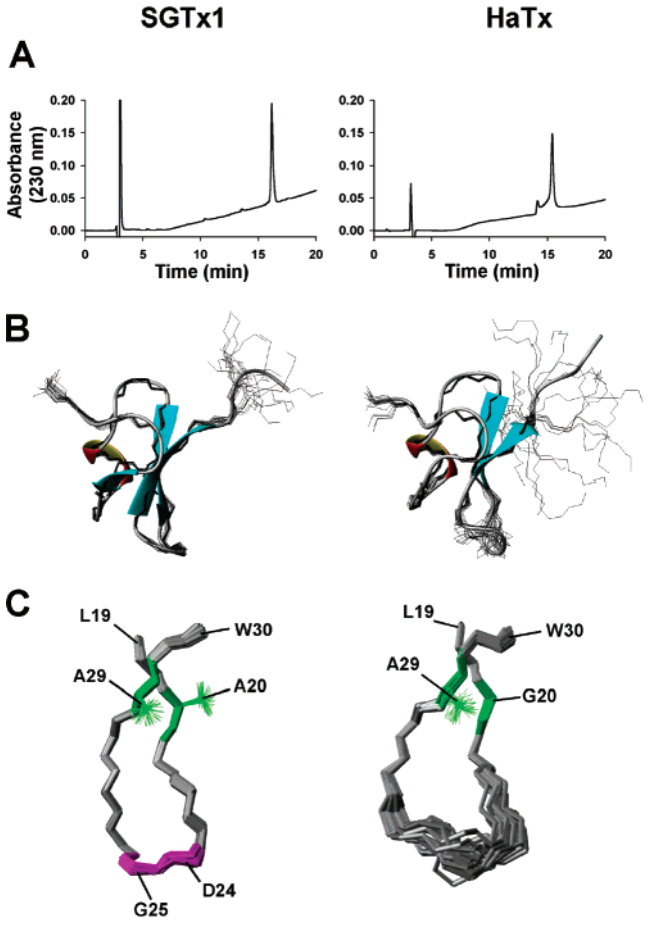

FIGURE 7: Comparison of synthetic SGTx1 and HaTx. (A) The chromatographic behavior of synthetic SGTx1 was compared to that of synthetic HaTx using a Shimadzu LC-6AD system with a C18 column (4.6 mm × 250 mm). The toxin was eluted with a linear gradient from 15 to 40% acetonitrile with 0.1% (v/v) TFA over 25 min at a flow rate of 1.0 mL/min, where mobile phase A was H_2O with 0.1% (v/v) TFA. (B) Ribbon representations and backbone heavy atoms (N, C^{α}, and C) of the converged structures of SGTx1 and HaTx are superimposed. The structural topology of the β-sheet and 3_{10}-helical turn was identified with MOLMOL. (C) Comparison of the β-hairpin regions (residues 19−30) of SGTx1 and HaTx. Residues important for the stability of the hairpin structure are colored purple (Asp24 and Gly25 of SGTx1) or green (residues 20 and 29 of SGTx1 and HaTx, respectively).

hydrophobic interaction between Ala20 and Ala29, which cannot occur in HaTx (Figure 7C). Gly is the most structurally unrestrained amino acid and usually breaks secondary structures. The β-hairpin, and in turn the overall conformation, of SGTx1 may thus be stabilized by two factors: adoption of a common sequence in the hairpin turn structure and interstrand hydrophobic interactions between two β-strands. Both of these influences are absent from the equivalent chain reversal in HaTx and thus may contribute to the observed conformational heterogeneity.

CONCLUSION

In this study, we investigated the three-dimensional structure of SGTx1 and the mechanism of its interaction with the Kv2.1 channel. SGTx1 is both structurally and functionally similar to HaTx, though detailed comparison of the structures of two molecules suggests that differences in the charge distribution at the binding surface and the amino acid composition of the β-hairpin structure likely account for the difference in their binding affinities for Kv2.1 channels and the decreased conformational heterogeneity of SGTx1.

As a new modifier of voltage-gated K^+ channel gating, SGTx1 appears to serve as a good substitute for HaTx. Further studies of structure−activity relationships of SGTx1 should improve our understanding of the gating mechanism in voltage-gated ion channels and provide a molecular basis for new peptide design.

ACKNOWLEDGMENT

We thank Prof. Ichio Shimada of The University of Tokyo (Tokyo, Japan) for valuable discussions.

REFERENCES

1. French, R. J., and Dudley, S. C., Jr. (1999) *Methods Enzymol. 294*, 575−605.
2. Ott, K. H., Becker, S., Gordon, R. D., and Ruterjans, H. (1991) *FEBS Lett. 278*, 160−166.
3. Hill, J. M., Alewood, P. F., and Craik, D. J. (1996) *Biochemistry 35*, 8824−8835.
4. Bontems, F., Roumestand, C., Gilquin, B., Me'nez, A., and Toma, F. (1991) *Science 254*, 1521−1523.
5. Davis, J. H., Bradley, E. K., Miljanich, G. P., Nadasdi, L., Ramachandran, J., and Basus, V. J. (1993) *Biochemistry 32*, 7396−7405.
6. Kohno, T., Kim, J. I., Kobayashi, K., Kodera, Y., Maeda, T., and Sato, K. (1995) *Biochemistry 34*, 10256−10265.
7. Farr-Jones, S., Miljanich, G. P., Nadasdi, L., Ramachandran, J., and Basus, V. J. (1995) *J. Mol. Biol. 248*, 106−124.
8. Swartz, K. J., and MacKinnon, R. (1997) *Neuron 18*, 665−673.
9. Swartz, K. J., and MacKinnon, R. (1997) *Neuron 18*, 675−682.
10. Li-smerin, Y., and Swartz, K. J. (2000) *J. Gen. Physiol. 115*, 673−684.
11. Rogers, J. C., Qu, Y., Tanada, T. N., Scheuer, T., and Catterall, W. A. (1996) *J. Biol. Chem. 271*, 15950−15962.
12. Winterfield, J. R., and Swartz, K. J. (2000) *J. Gen. Physiol. 116*, 637−644.
13. Jablonsky, M. J., Watt, D. D., and Krishna, N. R. (1995) *J. Mol. Biol. 248*, 449−458.
14. Manoleas, N., and Norton, R. S. (1994) *Biochemistry 33*, 11051−11061.
15. Kim, J. I., Konishi, S., Iwai, H., Kohno, T., Gouda, H., Shimada, I., Sato, K., and Arata, Y. (1995) *J. Mol. Biol. 250*, 659−671.
16. Takahashi, H., Kim, J. I., Min, H. J., Sato, K., Swartz, K. J., and Shimada, I. (2000) *J. Mol. Biol. 297*, 771−780.
17. Takeuchi, K., Park, E. J., Lee, C. W., Kim, J. I., Takahashi, H., Swartz, K. J., and Shimada, I. (2002) *J. Mol. Biol. 321*, 517−526.
18. Marvin, L., De, E., Cosette, P., Gagnon, J., Molle, G., and Lange, C. (1999) *Eur. J. Biolchem. 265*, 527−579.
19. Swartz, K. J., and MacKinnon, R. (1995) *Neuron 15*, 941−949.
20. Sasaki, T., Feng, Z.-P., Scott, R., Grigoriev, N., Syed, N. I., Fainzilber, M., and Sato, K. (1999) *Biochemistry 38*, 12876−12884.
21. Marion, D., and Wüthrich, K. (1983) *Biochem. Biophys. Res. Commun. 113*, 967−974.
22. Bax, A., and Davis, D. G. (1985) *J. Magn. Reson. 65*, 355−359.
23. Jeener, J., Meier, B. H., Bachmann, P., and Ernst, R. R. (1979) *J. Chem. Phys. 71*, 4546−4553.
24. Macura, S., Huang, Y., Suter, D., and Ernst, R. R. (1981) *J. Magn. Reson. 43*, 259−281.
25. Piotto, M., Saudek, V., and Sklenár, V. (1992) *J. Biomol. NMR 2*, 661−665.
26. Rance, M., Sørensen, O. W., Bodenhausen, G., Wagner, G., Ernst, R. R., and Wüthrich, K. (1983) *Biochem. Biophys. Res. Commun. 117*, 479−485.
27. Mueller, L. (1987) *J. Magn. Reson. 72*, 191−196.
28. Wüthrich, K., Billeter, M., and Braun, W. (1983) *J. Mol. Biol. 169*, 949−961.
29. Clore, M., Gronenborn, A. M., Nilges, M., and Ryan, C. A. (1987) *Biochemistry 26*, 8012−8023.
30. Nilges, M., Gronenborn, A. M., Brünger, A. T., and Clore, G. M. (1988) *Protein Eng. 2*, 27−38.
31. Pardi, A., Billerter, M., and Wüthrich, K. (1984) *J. Mol. Biol. 180*, 741−751.
32. Kline, A. D., Braun, W., and Wüthrich, K. (1988) *J. Mol. Biol. 204*, 675−724.
33. Hyberts, S. G., Marki, W., and Wagner, G. (1987) *Eur. J. Biochem. 164*, 625−635.
34. Wagner, G., Braun, W., Havel, T. F., Schaumann, T., Go, N., and Wüthrich, K. (1987) *J. Mol. Biol. 196*, 611−639.
35. Fletcher, J. I., Smith, R., O'Donoghue, S. I., Nilges, M., Conner, M., Howden, M. E. H., et al. (1997) *Nat. Struct. Biol. 4*, 559−566.
36. Fletcher, J. I., Chapman, B. E., Mackay, J. P., Howden, M. E. H., and King, G. F. (1997) *Structure 5*, 1525−1535.
37. Brünger, A. T. (1992) *X-PLOR Manual*, version 3.1, Yale University Press, New Haven, CT.
38. Laskowski, R. A., Rullmann, J. A., MacArthur, M. W., Kaptein, R., and Thornton, J. M. (1996) *J. Biomol. NMR 8*, 477−486.
39. Hutchinson, E. G., and Thornton, J. M. (1996) *Protein Sci. 5*, 212−220.
40. Koradi, R., Billeter, M., and Wüthrich, K. (1996) *J. Mol. Graphics 14*, 29−32.
41. Hyberts, S. G., Goldberg, M. S., Havel, T. F., and Wagner, G. (1992) *Protein Sci. 1*, 736−751.
42. Frech, G. C., VanDongen, A. M., Schuster, G., Brown, A. M., and Joho, R. H. (1989) *Nature 340*, 642−645.
43. Li-Smerin, Y., and Swartz, K. J. (1998) *Proc. Natl. Acad. Sci. U.S.A. 95*, 8585−8589.
44. Aggarwal, S. K., and MacKinnon, R. (1996) *Neuron 16*, 1169−1177.
45. Garcia, M. L., Garcia-Calvo, M., Hidalgo, P., Lee, A., and MacKinnon, R. (1994) *Biochemistry 33*, 6834−6839.
46. Wüthrich, K. (1986) *NMR of Proteins and Nucleic Acids*, Wiley & Sons, New York.
47. Richardson, J. S. (1981) *Adv. Protein Chem. 34*, 167−339.
48. Pallaghy, P. K., Nielsen, K. J., Craik, D. J., and Norton, R. S. (1994) *Protein Sci. 3*, 1833−1839.
49. Norton, R. S., and Pallaghy, P. K. (1998) *Toxicon 36*, 1573−1583.
50. Singh, J., and Thornton, J. M. (1985) *FEBS Lett. 191*, 1−6.
51. Li-Smerin, Y., and Swartz, K. J. (2001) *J. Gen. Physiol. 117*, 205−217.
52. Jiang, Y., Lee, A., Chen, J., Ruta, V., Cadene, M., Chait, B. T., and MacKinnon, R. (2003) *Nature 423*, 33−41.
53. Shiau, Y. S., Lin, T. B., Liou, H. H., Huang, P. T., Lou, K. L., and Shiau, Y. Y. (2002) *J. Mol. Model. 8*, 253−257.
54. Lou, K. L., Huang, P. T., Shiau, Y. S., and Shiau, Y. Y. (2002) *J. Mol. Recognit. 15*, 175−179.
55. Blanco, F., Ramirez-Alvarado, M., and Serrano, L. (1998) *Curr. Opin. Struct. Biol. 8*, 107−111.
56. Wishart, D. S., Sykes, B. D., and Richards, F. M. (1992) *Biochemistry 31*, 1647−1651.
57. Brooks, B. R., Bruccoleri, R. E., Olafson, B. D., States, D. J., Swaminathan, S., and Karplus, M. (1983) *J. Comput. Chem. 4*, 187−217.

BI0353373